NANOSYSTEMS:
PHYSICS, CHEMISTRY, MATHEMATICS

Original article

Bugrov A.N., et al. *Nanosystems: Phys. Chem. Math.*, 2025, **16** (6), 850–864.
http://nanojournal.ifmo.ru
DOI 10.17586/2220-8054-2025-16-6-850-864

Synthesis, structure and properties of composite proton-conducting membranes based on a Nafion-type perfluorinated copolymer with $Zr_{1-x}Y_xO_{2-0.5x}$ nanoparticles

Alexander N. Bugrov[1,2,a], Galina N. Gubanova[1,b], Oleg N. Primachenko[1,c], Iosif V. Gofman[1,d], Elena M. Ivan'kova[1,e], Elena N. Popova[1,f], Demid A. Kirilenko[3,g], Victor K. Lavrentyev[1,h], Elena N. Vlasova[1,i], Svetlana V. Kononova[1,j]

[1]NRC "Kurchatov Institute" – PNPI – IMC, St. Petersburg, Russia

[2]St. Petersburg Electrotechnical University "LETI", St. Petersburg, Russia

[3]Ioffe Institute, St. Petersburg, Russia

[a]bugrov.an@mail.ru, [b]gubanovagn@yandex.ru, [c]alex-prima@mail.ru, [d]gofman@imc.macro.ru, [e]ivelen@mail.ru, [f]men682003@mail.ru, [g]demid.kirilenko@mail.ioffe.ru, [h]lavrentev1949@mail.ru, [i]evl021960@gmail.com, [j]svetlanavkononova@gmail.com

Corresponding author: Alexander N. Bugrov, bugrov.an@mail.ru

PACS 61.46.+w, 82.33.Pt, 68.35.Dv

ABSTRACT $Zr_{1-x}Y_xO_{2-0.5x}$ nanoparticles were introduced into the sulfonic acid form of the Nafion-type perfluorinated copolymer prior to membrane formation to improve its water retention, thermal stability, and proton conductivity. Since the conditions under which nanoparticles are formed can significantly influence their size, phase composition, morphology, and surface chemistry, various approaches to filler synthesis were considered in this study. It was found that among the wet-chemical methods used to produce zirconia-based nanoparticles, solvothermal synthesis offers the most promise in terms of increasing the surface proton conductivity of composite membranes. This method ensures small size, large specific surface area, and high hydrophilicity of the nanoparticles. Consequently, their incorporation into a Nafion-type perfluorinated copolymer increases the membrane's moisture retention and improves to its proton-conducting properties. In the case of $Zr_{1-x}Y_xO_{2-0.5x}$ nanoparticles formed under solution combustion conditions, their more hydrophobic surface did not contribute to an increase in the moisture content of the perfluorinated copolymer, but did allow its maximum operating temperature to be increased by 20 °C.

KEYWORDS proton conductivity, impedance spectroscopy, yttria-stabilized zirconia, glycine-nitrate combustion, sol-gel, hydrothermal synthesis, solvothermal method

ACKNOWLEDGEMENTS The authors thank D. A. Gavrilova, M. A. Gavrilova, and N. S. Kormiltsina, students of the St. Petersburg State Institute of Technology (Technical University), for their assistance in determining the conditions for producing nanoparticles. The authors also thank senior researcher G. V. Vaganov and senior laboratory assistant V. D. Vavilova from the NRC "Kurchatov Institute" – PNPI – IMC for measuring the contact angle of the composite membranes and determining their bulk proton conductivity, respectively. X-ray diffraction analysis was performed using equipment from the Engineering Center of the Saint Petersburg State Institute of Technology. TEM studies were performed using equipment of the Federal Joint Research Center "Material science and characterization in advanced technology" supported by the Ministry of Education and Science of the Russian Federation. The research work was carried out within the framework of State Programs of Branch of Petersburg Nuclear Physics Institute named by B. P. Konstantinov of National Research Centre "Kurchatov Institute" – Institute of Macromolecular Compounds (Project 122012000452-9).

FOR CITATION Bugrov A.N., Gubanova G.N., Primachenko O.N., Gofman I.V., Ivan'kova E.M., Popova E.N., Kirilenko D.A., Lavrentyev V.K., Vlasova E.N., Kononova S.V. Synthesis, structure and properties of composite proton-conducting membranes based on a Nafion-type perfluorinated copolymer with $Zr_{1-x}Y_xO_{2-0.5x}$ nanoparticles. *Nanosystems: Phys. Chem. Math.*, 2025, **16** (6), 850–864.

1. Introduction

Proton exchange membrane fuel cells are promising, environmentally friendly electrochemical power sources that are characterized by increased energy density and relatively high power generation efficiency [1]. The most commonly used membranes in fuel cells are Nafion-type membranes due to their mechanical strength, chemical resistance, high selectivity and proton conductivity in the hydrated state [2, 3]. The microstructure of the Nafion membrane is a network of

interconnected clusters of sulfonic acid groups (proton exchange channels) that are formed in a hydrophobic polymer matrix of polytetrafluoroethylene with hydrophilic perfluorinated side chains containing ionic groups [4,5]. Proton migration in membranes of this type depends significantly on the water content [6]. At high temperatures, the Nafion membrane loses moisture, which leads to irreversible mechanical damage and a decrease in proton conductivity. The maximum proton conductivity is achieved when the Nafion membrane is fully hydrated. The use of this membrane in methanol fuel cells is further limited by the permeability of methanol, the incomplete oxidation of which promotes the release of CO, which deactivates the platinum catalyst at the anode. Therefore, in order to maintain high proton conductivity, improve the kinetics of oxidation-reduction reactions at both electrodes, protect the platinum catalyst, and optimize the balance between operating temperature and humidity of the polymer electrolyte membrane in fuel cells [7], approaches have been developed to increase its water retention [8]. One such approach is the physicochemical design of new polymer-inorganic composite membranes capable of effectively binding water within their structure, absorbing moisture, reducing the degree of fuel-oxidizer mixing and electroosmotic resistance in the system, and increasing proton conductivity. At the same time, they must also maintain their mechanical strength, thermal stability and chemical resistance, under conditions of high operating temperatures [9] and low relative humidity [10]. Basically, to retain water in the membrane under high-temperature operating conditions, various types of inorganic fillers were used due to their electrostatic attraction within the double electric layer [11], anti-swelling and hydrophilic properties [12–14]. Moreover, the hydrated water on the surface of such particles can form bridges between clusters of sulfonic acid groups, which can provide additional pathways for proton transfer [17]. The introduction of inorganic fillers, such as silica (SiO_2) [18, 19], titania (TiO_2) [20, 21], ceria (CeO_2) [22], zirconia (ZrO_2) [23, 24] and zeolites [25] allows you to regulate the swelling degree of membranes, change their mechanical properties, as well as the structure of pores and channels, which helps to increase proton conductivity of fuel cells [26–28]. Among the above-mentioned fillers for proton-conducting membranes, nanosized additives based on zirconia have proven to be the most effective. In [10], hybrid polymer-inorganic membranes based on Nafion and four types of oxide nanoparticles (ZrO_2, TiO_2, ZrO_2–TiO_2, ZrO_2–Y_2O_3) were fabricated using the doctor blade method for use as electrolytes in medium-temperature fuel cells with a proton exchange membrane. Pristine, sulfated and phosphated zirconia nanoparticles were used to modify the Nafion membrane to improve water retention, thermal stability, proton conductivity, and reduce methanol permeability [29]. In this study, inorganic nanoparticles were introduced into Nafion using remelting, swelling-impregnation, and ion exchange methods. The proton conductivity of the membrane with 5 wt. % sulfated ZrO_2 exceeded 0.103 S/cm at room temperature and had the highest water absorption rate – 35 %.

It is known that ZrO_2 can be represented by three polymorphic modifications: monoclinic, tetragonal and cubic [30]. Of particular interest among the crystal structures of zirconia are the tetragonal and cubic phases (t, c-ZrO_2) due to their high oxygen-ion conductivity and chemical resistance over a wide range of temperatures and oxygen partial pressures. Therefore, they are a well-known candidate for applications such as the development of fuel cells [31]. To obtain nanoparticles of ZrO_2 high-temperature modifications, stabilizer ions such as calcium (Ca^{2+}), europium (Eu^{3+}), or yttrium (Y^{3+}) are introduced into its structure, which prevent phase transitions upon cooling [32]. The crystal structure, size, shape, and surface chemistry of zirconia nanoparticles are typically determined by the synthesis and thermal treatment methods [33, 34]. Therefore, in this study, t, c-ZrO_2 nanoparticles were obtained using various synthesis techniques, characterized by a combination of physicochemical analysis methods and subsequently used as a modifying additive for Nafion-type proton-conducting membrane.

2. Experimental

2.1. Materials

The following reagents were used for the synthesis of $Zr_{1-x}Y_xO_{2-0.5x}$ nanoparticles: $ZrOCl_2 \times 8H_2O$ (CAS: 13520-92-8, Lenreaktiv, Russia, pure), $ZrO(NO_3)_2 \times 2H_2O$ (CAS: 14985-18-3, Lenreaktiv, Russia, pure), $Zr(OC_4H_9)_4$ (CAS: 1071-76-7, Sigma-Aldrich, 80 % Gew.Lsg.in 1-Butanol), $Y(NO_3)_3 \times 6H_2O$ (CAS: 13494-98-9, Vekton, Russia, chemically pure), $YCl_3 \times 6H_2O$ (CAS: 10025-94-2, Vekton, Russia, pure), ammonia solution (Vekton, CAS: 1336-21-6, 25 % , chemically pure) and C_2H_5OH (CAS: 64-17-5, Ekroskhim, Russia, 99.5 %).

The Nafion-type membrane (LSC-1) based on a precursor copolymer was obtained by aqueous emulsion copolymerization of tetrafluoroethylene with the perfluorinated monomer perfluoro(3,6-dioxa-4-methyl-7-octene)sulfonyl fluoride using the technology described in detail in [35]. A copolymer with equivalent mass values (molecular mass of a polymer chain fragment per sulfonic acid group) of 1030 g-eq/mol SO_3H groups was used as the base chemical structure.

N,N-dimethylformamide (CAS: 68-12-2, Vekton, Russia, extra pure) was used as a solvent in the dispersion preparation of the LSC-1 copolymer in sulfonic acid form.

2.2. Synthesis of $Zr_{1-x}Y_xO_{2-0.5x}$ nanoparticles

2.2.1. Glycine-nitrate combustion. Zirconium (6.58 mmol) and yttrium (0.42 mmol) nitrates were dissolved in 50 ml of water with the addition of 5 ml of concentrated nitric acid, vigorously stirred, and heated in the presence of glycine. The ratio of the glycine mole number to the total metal nitrate mole ones in the reaction mixture was 1.3. After homogenization of the reaction mixture, the solution was placed in a sand bath and heated until ignition occurred. The combustion product,

a gray foam-like substance, was ground in an agate mortar to a powder and annealed in a muffle furnace at 500 °C for 2 hours.

2.2.2. Sol-gel synthesis. 25 ml of 0.02 M $Y(NO_3)_3 \times 6H_2O$ solution was added to 36 ml of 80 % $Zr(OC_4H_9)_4$ zirconium butoxide. The resulting mixture was vigorously stirred at 60 °C for 1 hour. The resulting sol was dried to form a gel and heat-treated at 700 °C for 2 hours. The resulting product was ground in agate mortar to a powder.

2.2.3. Hydrothermal synthesis. $ZrOCl_2 \times 8H_2O$ (6.58 mmol) and $YCl_3 \times 6H_2O$ (0.42 mmol) were dissolved in distilled water and stirred. The corresponding metal hydroxides were then coprecipitated by adding 25 % ammonia solution dropwise to the dissolved reagents with continuous stirring until a white, curdy precipitate formed at pH of 14. The resulting precipitate was then repeatedly washed by decantation until a negative chloride ion reaction was achieved and dried to constant weight at 100 °C. The resulting white powder was poured into an autoclave cell and filled with water. The hydrothermal vessel containing the mixture was then sealed and maintained at 200 °C for 4 hours. The particles formed under hydrothermal conditions were removed from the cell and dried in air at 100 °C.

2.2.4. Solvothermal synthesis. $YCl_3 \times 6H_2O$ (0.5 mmol) dissolved in 15 ml of ethanol was added in small portions to $Zr(OC_4H_9)_4$ (7.7 mmol) with constant stirring. After thorough stirring for 90 minutes, the resulting suspension was placed in an autoclave. The synthesis was carried out for 72 hours at an isothermal holding temperature of 200 °C. The precipitate was then separated from the mother liquor and washed repeatedly with distilled water by centrifugation. The washed precipitate was dried at 100 °C and then heat-treated at 500 °C for 2 hours. The annealed sample was ground to a powder.

2.3. Preparation of composite films

A method for introducing zirconia-based nanoparticles into Nafion-type perfluorinated copolymer dispersions for the subsequent fabrication of composite membranes was developed. Nafion-type (LSC-1) copolymer powders in sulfonic acid form were used as a matrix. To obtain composite membranes, dispersions of ZrO_2-based nanoparticles in N,N-dimethylformamide (DMF) with an LSC-1 concentration of no more than 5 wt. % were prepared, enabling the production of fairly uniform film materials using a casting method. The kinematic viscosity of the dispersions was crucial for the formation of cast composite membranes with a smooth surface. Nanoparticle dispersions in solution were prepared in a glass flask with stirring at 1000 rpm and ultrasonic treatment (3.5 kHz, 50 W) for 30 minutes. The nanoparticle dispersion was then added to a pre-obtained LSC-1 one in DMF and stirred magnetically for 5 min. The ZrO_2-based nanoparticle content in the LSC-1 composite membranes was 0.5 wt. % . Composite membranes were formed on a glass substrate using the casting method with solvent removal under an IR lamp at 80 °C for 4 hours. The composite membrane was then evacuated to remove residual solvent and annealed at 100 °C for 3 hours. Before measuring the proton conductivity of the composite membranes using impedance spectroscopy, they were rinsed with a 15 % nitric acid solution and then with distilled water to neutral pH.

2.4. Research methods

2.4.1. X-ray phase analysis. X-ray phase analysis of $Zr_{1-x}Y_xO_{2-0.5x}$ nanoparticles synthesized by glycine-nitrate combustion and wet-chemical methods was performed using a Rigaku SmartLab 3 X-ray diffractometer (CuK_α, 40 kV, 44 mA) in the 10 – 70° range with a scan rate of 0.5 °/min. Full-profile analysis of X-ray diffraction (XRD) patterns of nanoparticle powders was performed using the PD-Win 4.0 software package (Research and Production Association "Burevestnik", Russia). X-ray phase analysis of the samples was carried out by the Crystallographica Search-Match software package (Oxford Cryosystems, UK) based on the obtained values of interplanar distances, peak widths at half-height, their intensity and position (2θ) using the ICDD PDF-2 database. The average crystallite sizes for nanopowders were estimated based on the broadening of XRD peaks using the Scherrer formula. The MAUD software package (L. Lutterotti, Italy) was used to determine the phase composition and calculate the parameters of a unit cell of nanoparticles [36].

Structural studies of the membranes were performed using a DRON-2.0 automated X-ray diffractometer manufactured by the Leningrad Research and Production Association "Burevestnik". CuK_α radiation was used. Monochromatization was achieved with a Ni filter. The images were taken in transmission mode. The crystallinity degrees of the samples were determined by the ratios of the integral intensities of crystalline reflections and amorphous halo.

2.4.2. Transmission electron microscopy. Transmission electron microscopy (TEM; JEOL JEM-2100F) with an accelerating voltage of 200 kV was used to determine the shape and size of $Zr_{1-x}Y_xO_{2-0.5x}$ nanoparticles. Sample preparation for TEM included the deposition of oxide nanoparticle dispersions onto graphene-coated copper grids and subsequent water removal from them during the drying process [37].

2.4.3. Energy-dispersive X-ray spectroscopy. The elemental composition of synthesized nanoparticles was measured using a Hitachi S-570 (Tokyo, Japan) scanning electron microscope with a Bruker Quantax 200 microanalysis system (Bruker Corporation, USA). Quantitative energy-dispersive X-ray (EDX) spectroscopy was carried out using the method of fundamental parameters. The standard accumulation time of the spectrum was 60 seconds. The composition was determined from the maximum possible area of the test sample.

2.4.4. FTIR spectroscopy. The amount of hydroxyl groups on the surface of the synthesized $Zr_{1-x}Y_xO_{2-0.5x}$ nanoparticles was estimated using FTIR spectroscopy on a Vertex 70 spectrometer (Bruker Optik GmbH, Ettlingen, Germany), which is equipped with an attenuated total reflectance device (Pike Technologies Inc., Madison, WI 53719, USA).

2.4.5. Scanning electron microscopy. The degree of nanoparticle dispersion and the uniformity of their distribution within the polymer matrix were studied by analyzing micrographs of transverse fractures of composite films in liquid nitrogen using a SUPRA 55VP scanning field-emission electron microscope (Carl Zeiss, Germany). Prior to analysis, a conductive platinum coating was applied to the surface of the samples using vacuum deposition.

2.4.6. Determination of the surface wetting angle of composite films. The wetting of the surface of composite films with water was assessed by the sessile drop method using a DSA 30 device (Kruss, Germany).

2.4.7. Thermogravimetric analysis. Thermogravimetric analysis (TGA) of membrane samples was performed using a Netzsch TG 209 F1 (Germany) in a temperature range from ambient to 800 °C at a heating rate of 10 °C/min under an inert gas flow. The test samples weighed between 2 and 3 mg. Processes associated with heat release or absorption during membrane heating were studied using differential scanning calorimetry using a Netzsch DSC 204 F1 (Germany) in a temperature range from room temperature to 280 °C (below the decomposition temperature of sulfo groups) under an argon atmosphere (argon flow rate: 25 ml/min, heating rate: 10 °/min).

2.4.8. Differential scanning calorimetry. Processes associated with heat release or absorption during membrane heating were studied using differential scanning calorimetry using a Netzsch DSC 204 F1 (Germany) in a temperature range from room temperature to 280 °C (below the decomposition temperature of sulfo groups) under an argon atmosphere (argon flow rate: 25 ml/min, heating rate: 10 °/min).

2.4.9. Mechanical testing of films. Mechanical tests of the unfilled and composite films were conducted in uniaxial tension using an AG-100X Plus universal mechanical testing rig (Shimadzu Corp., Japan). The following material properties were determined during testing: elastic modulus (E), plastic yield limit (σ_y), strength (σ_p), and ultimate strain before failure (ε_p).

2.4.10. Impedance spectroscopy. Surface proton conductivity was measured by impedance spectroscopy at equilibrium membrane saturation with water, i.e., at the maximum water content achieved by boiling at 100 °C for 1 hour. A Z-3000X impedance meter (Elins, Russia) with a 4-electrode measuring cell and a frequency range of 10 – 150 kHz was used. Specific electrical conductivity (σ_n) was calculated using the following formula:

$$\sigma_n = L/(R_m \cdot h \cdot b), \tag{1}$$

where L is the distance between the voltage electrodes of the measuring cell (L = 1.77 cm according to the measuring cell specifications), cm; h is the average membrane thickness, cm; b is the average membrane width, cm; R_m is the membrane resistance, Ohm.

The bulk proton conductivity of the membranes was measured in a two-electrode cell using an Elins Z-1500J impedance meter at an initial frequency of 3 kHz and a final ones of 100 kHz. The equilibrium moisture content of the membranes was determined by the weight of the samples, which were dried to constant weight in a vacuum at 80 °C and then subjected to equilibrium saturation in water for 24 hours at 20 °C. Before measurements, the sample was soaked in distilled water for at least 15 minutes, after which it was additionally moistened as measurements were taken. During the measurements, the sample was heated from 25 to 120 °C, with instrument readings taken every 5 °C.

3. Results and discussion

Powders of $Zr_{1-x}Y_xO_{2-0.5x}$ nanoparticles were obtained using solution combustion and wet chemistry methods. According to XRD data, the products formed from zirconium and yttrium nitrate solutions with glycine during combustion synthesis, after their annealing and grinding to a powder state, were a mixture of ZrO_2 nanocrystals of the tetragonal (t) and cubic (c) phases in a ratio of 40:60 (Table 1). A qualitative XRD analysis carried out in the PD-Win 4.0 and Crystallographica Search-Match software packages showed the best correspondence of the synthesized nanocrystalline powder to card No. 49-1642 for c-ZrO_2 from the ICDD PDF-2 database (Fig. 1a). Refinement of the unit cell parameters using the Rietveld method, performed in the MAUD software package, showed that the values of the lattice periods a, b and c for the synthesized ZrO_2 nanocrystals calculated from XRD patterns differ from those given in the literature [38] in the case of thermally stabilized tetragonal phase (Table 1). This fact indicates the incorporation of Y^{3+} ions into the crystal lattice of t-ZrO_2 and the formation of $Zr_{1-x}Y_xO_{2-0.5x}$ solid solutions. A similar conclusion can be made for cubic phase nanocrystallites formed during glycine-nitrate combustion of the reaction mixture, the cell parameters of which were almost identical to those recorded in the literature for stabilized c-ZrO_2 [39]. The average size of the coherent scattering regions (CSRs) for the $Zr_{1-x}Y_xO_{2-0.5x}$ nanoparticles powders obtained by solution combustion, calculated using the Scherrer formula, was 10±2 nm. For tetragonal and cubic ZrO_2 crystallites separated in the MAUD software package, the CSR region sizes were 6 and 31 nm, respectively. According to TEM data, the nanopowder contained mono- and polycrystalline quasi-spherical particles with sizes of 3 – 5 and 8 – 18 nm, respectively (Fig. 2a).

TABLE 1. XRD data for nanoparticles of $Zr_{1-x}Y_xO_{2-0.5x}$ solid solutions obtained by different synthesis methods

Preparation method	$Zr_{1-x}Y_xO_{2-0.5x}$						
	Polymorphic modification	Phase content, vol. %	Unit cell parameters		Microstresses	Average crystallite size, nm	
			lengths	angles		MAUD	PDWin
Literary data [38, 39]	Tetragonal	–	$a = b = 3.612$ $c = 5.212$	$\alpha = \gamma = \beta = 90$	–	–	–
	Cubic	–	$a = b = c =$ 5.129	$\alpha = \gamma = \beta = 90$	–	–	–
Glycine-nitrate combustion	Monoclinic	–	–	–	–	–	–
	Tetragonal	40	$a = b = 3.623 \pm 0.001$ $c = 5.171 \pm 0.002$	$\alpha = \gamma = \beta = 90$	$5.9\times10^{-4}\pm$ 2×10^{-4}	6 ± 1	10 ± 2
	Cubic	60	$a = b = c =$ 5.127 ± 0.001	$\alpha = \gamma = \beta = 90$	$0.0047\pm$ 2×10^{-5}	31 ± 2	
Sol-gel	Monoclinic	–	–	–	–		–
	Tetragonal	76	$a = b = 3.611 \pm 0.001$ $c = 5.171 \pm 0.001$	$\alpha = \gamma = \beta = 90$	$0.002\pm$ 2.8×10^{-5}	57 ± 6	22 ± 4
	Cubic	24	$a = b = c =$ 5.134 ± 0.001	$\alpha = \gamma = \beta = 90$	$0.0073\pm$ 9×10^{-4}	6 ± 2	
Hydrothermal synthesis	Monoclinic	–	–	–	–		–
	Tetragonal	82	$a = b = 3.466 \pm 0.02$ $c = 5.682 \pm 0.056$	$\alpha = \gamma = \beta = 90$	$0.11\pm$ 0.001	–	3 ± 1
	Cubic	18	$a = b = c =$ 5.151 ± 0.003	$\alpha = \gamma = \beta = 90$	$0.018\pm$ 0.0002	–	
Solvothermal synthesis	Monoclinic	–	–	–	–	–	–
	Tetragonal	83	$a = b = 3.415 \pm 0.003$ $c = 5.773 \pm 0.022$	$\alpha = \gamma = \beta = 90$	$0.109\pm$ 0.001	–	3 ± 1
	Cubic	17	$a = b = c =$ 5.131 ± 0.004	$\alpha = \gamma = \beta = 90$	$0.024\pm$ 3.8×10^{-4}	–	

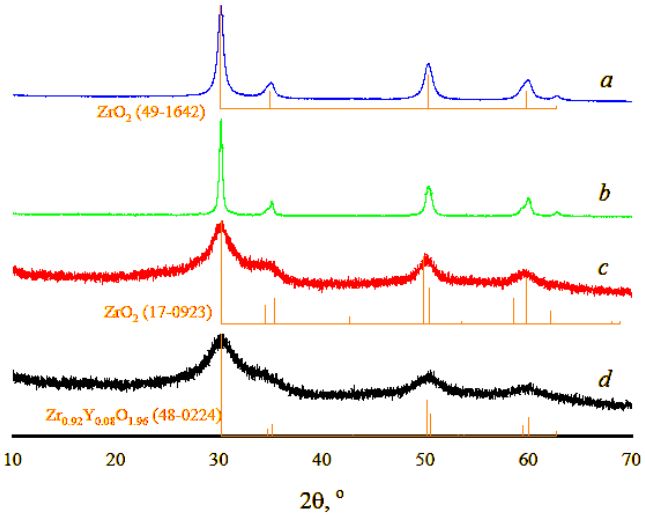

FIG. 1. Comparison with a ICDD PDF-2 database of the XRD patterns of $Zr_{1-x}Y_xO_{2-0.5x}$ nanoparticles obtained by different methods: glycine-nitrate combustion (a), sol-gel (b), hydrothermal (c) and solvothermal syntheses (d)

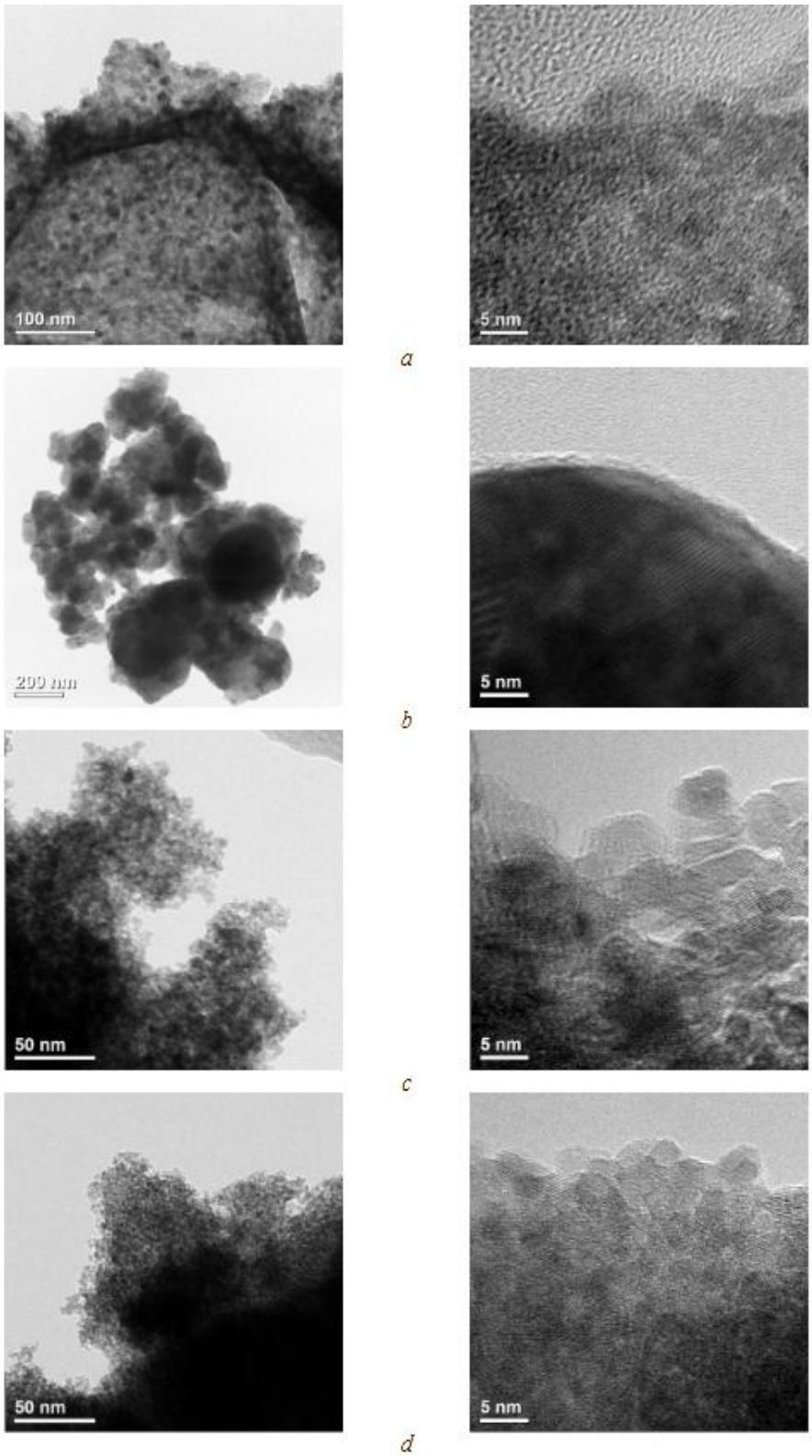

FIG. 2. TEM micrographs of $Zr_{1-x}Y_xO_{2-0.5x}$ nanoparticles obtained by different methods: glycine-nitrate combustion (a), sol-gel (b), hydrothermal (c) and solvothermal syntheses (d)

TABLE 2. Elemental composition of $Zr_{1-x}Y_xO_{2-0.5x}$ nanoparticles obtained by various synthesis methods

Preparation method	at. %	
	Y	Zr
Glycine-nitrate combustion	3.54±0.05	96.46±0.05
Sol-gel	6.9±0.33	93.1±0.33
Hydrothermal synthesis	5.06±0.02	94.94±0.02
Solvothermal synthesis	3.91±0.05	96.09±0.05

Aging of the gel formed by mixing yttrium nitrate and zirconium butoxide solutions, its subsequent annealing at 700 °C for 2 hours, and disintegration yielded t- and c-ZrO_2 nanoparticles in a 76:24 ratio. The average crystallite size, calculated from a full-profile analysis of the nanoparticle X-ray diffraction pattern, was 22±4 nm (Fig. 1b). Qualitative X-ray diffraction analysis of the sample in Crystallographica Search-Match showed the best match for t-ZrO_2 (card No. 48-224). The average crystallite size, calculated using the MAUD program, was 60 nm for $t-ZrO_2$, while for the cubic modification it was an order of magnitude smaller (Table 1). Refinement of the crystal lattice parameters using the Rietveld method revealed that the a and b values correspond to those reported in the literature for undoped t-ZrO_2, while the lattice constant c for the synthesized tetragonal phase nanoparticles was lower [38]. In turn, the calculated unit cell parameters for the cubic phase of $Zr_{1-x}Y_xO_{2-0.5x}$ nanoparticles were higher than those presented in [39] for c-ZrO_2. TEM (Fig. 2b) demonstrated that sol-gel synthesis resulted in the formation of quasi-spherical particles, representing intergrowths of crystallites, with a wide grain size distribution (from 40 to 300 nm).

Qualitative XRD analysis showed that hydrothermal treatment (200 °C, 70 MPa, 4 hours) of a mixture of yttrium and zirconium hydroxides coprecipitated from their chloride solutions using NH_4OH, similar to the previous synthesis method, yielded crystals of t- (82 %) and c-ZrO_2 (18 %) (Fig. 1c). The average crystallite size, calculated from the diffraction maxima of t-/ c-ZrO_2 using the Scherrer formula, was 3±1 nm. It was not possible to determine the separate crystallite sizes of the tetragonal and cubic phases using the MAUD program. The formation of a $Zr_{1-x}Y_xO_{2-0.5x}$ solid solution is indicated by a decrease in the a and b parameters of the unit cell with a significant increase in the lattice constant c, compared to the crystallographic data for t-ZrO_2 given in the literature (Table 1) [38]. For cubic phase crystallites formed under hydrothermal conditions, the lattice parameters were higher than for solid solution samples obtained at temperatures up to 1400 K [39]. Spherical $Zr_{1-x}Y_xO_{2-0.5x}$ nanoparticles with an average diameter of 4±1 nm were observed in the TEM micrographs (Fig. 2c). It should be noted that the diameter of the nanoparticles formed under hydrothermal conditions is comparable with the average size of the CSRs within the error limits, i.e., they are single-crystal.

A similar isothermal holding at 200 °C for 24 hours of a pre-homogenized mixture of zirconium alkoxide and an alcoholic solution of yttrium chloride also promoted the crystallization of nanoparticles of the $Zr_{1-x}Y_xO_{2-0.5x}$ solid solutions (Table 1). The ratio of crystalline phases in the nanoparticle powder obtained by solvothermal synthesis (SS) was practically the same as that obtained during hydrothermal treatment of the $ZrO(OH)_2$–$Y(OH)_3$ precipitate. The average crystallite size was 3±1 nm, which coincided with the particle diameter in the TEM micrographs (Fig. 2d).

EDX spectroscopy results showed that the yttrium content in the resulting $Zr_{1-x}Y_xO_{2-0.5x}$ solid solution nanoparticles was lower than the synthesis target for virtually all methods used, except sol-gel (SG) technology (Table 2). According to the phase diagrams of ZrO_2-Y_2O_3, at yttria concentrations below 3 mol. % , solid solution crystals form, corresponding predominantly to the tetragonal structure of zirconium dioxide [40,41]. This is consistent with the results of our quantitative X-ray phase analysis for all solid solution samples obtained by wet chemistry methods. In the case of glycine-nitrate combustion, due to the high rate of particle formation and the high synthesis temperature, they crystallize predominantly as the cubic polymorph of ZrO_2.

A study using FTIR spectroscopy of the surface chemistry of $Zr_{1-x}Y_xO_{2-0.5x}$ nanoparticles obtained by different methods showed that in the case of hydro- and solvothermal treatment of precursors of both inorganic and organic nature, fillers with a more hydrophilic surface are formed. The integrated intensity of the bands corresponding to the stretching and bending vibrations of OH groups in the range of 3700 – 2690 cm^{-1} and at 1615 cm^{-1} for nanoparticles obtained by the two aforementioned synthesis methods is significantly higher than that in the FTIR spectra of similar systems formed via the sol-gel process or solution combustion (Fig. 3). This circumstance may be useful from the point of view of moisture retention by the surface of $Zr_{1-x}Y_xO_{2-0.5x}$ nanoparticles, which will increase the operating temperature of Nafion-type perfluorinated membranes by introducing a filler.

SEM micrographs of composite film cross-sections were analyzed to control the dispersion degree and distribution homogeneity of $Zr_{1-x}Y_xO_{2-0.5x}$ nanoparticles in the bulk of the Nafion-type polymer matrix. Nanoparticles obtained by hydrothermal synthesis (HS), with a large number of hydroxyl groups on the surface and a small crystallite size, aggregated less and were more uniformly distributed within the perfluorinated polymer (Fig. 4a). Meanwhile, $Zr_{1-x}Y_xO_{2-0.5x}$

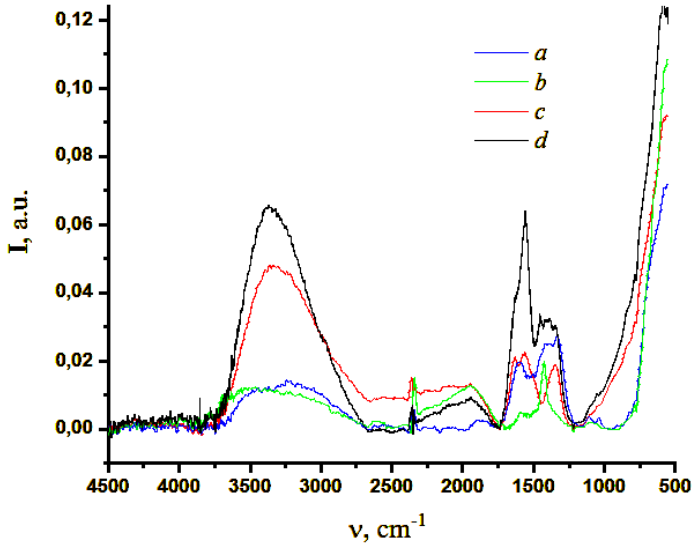

FIG. 3. FTIR spectroscopy of $Zr_{1-x}Y_xO_{2-0.5x}$ nanoparticles obtained by different methods: glycine-nitrate combustion (a), sol-gel (b), hydrothermal (c) and solvothermal (d) syntheses

nanoparticles, formed from zirconium butoxide and yttrium chloride under solvothermal conditions with similar dimensions and a higher surface hydrophilicity, agglomerated intensely within the same polymer and collected in its near-surface layer as large aggregates (Fig. 4b). It should be noted that the majority of the agglomerated particles protruded onto the surface of the composite film. This is probably due to differences in the density of the perfluorinated copolymer and inorganic fillers during the formation of composite membranes. The introduction of nanoparticles obtained using sol-gel technology into the polymer matrix also resulted in strong filler aggregation, but the number of aggregates near the surface was significantly smaller and was hidden beneath the polymer layer (Fig. 4c). The greatest incompatibility between the perfluorinated polymer and $Zr_{1-x}Y_xO_{2-0.5x}$ nanoparticles was observed when the latter were produced using the glycine-nitrate combustion (GNC) method (Fig. 4d). The incorporation of these particles into the polymer was accompanied by the formation of aggregates ranging from a few to tens of microns in size, which settled under their own weight. Therefore, a micrograph of a composite film cleavage shows a gradient in the distribution of aggregates with an increasing concentration toward the substrate on which it was formed, while it is clearly visible that they remain beneath the polymer layer.

Determining the surface contact angle of composite films using the sessile drop method revealed that samples containing $Zr_{1-x}Y_xO_{2-0.5x}$ nanoparticles with a high number of OH groups are more hydrophilic. When a drop was applied to the film surface of a perfluorinated copolymer containing 0.5 wt. % nanoparticles obtained under hydrothermal conditions, its instant swelling was observed (Fig. 5).

Thermogravimetric analysis (TGA) of composite films based on a perfluorinated copolymer incorporating $Zr_{1-x}Y_xO_{2-0.5x}$ nanoparticles with different chemical prehistory revealed three main processes occurring during heating. The first step of mass loss recorded on the TGA curves in the range from room temperature to 180 – 200 °C is associated with the release of water and residual DMF solvent (the boiling point of the solvent is 155.5 °C). A subsequent increase in temperature facilitated the decomposition of sulfo groups in the range from 300 to 420 °C. We believe that the most reasonable parameter for the thermal stability of composite membranes is the temperature corresponding to the maximum mass loss during the destruction of the sulfo-containing fragment (T2 in Table 3), determined based on analysis of the differential thermogravimetric curves. The third stage of intense mass loss began around 400 °C and continued until ∼600 °C, that is, until virtually complete polymer degradation. This final stage was associated with the destruction of the membrane side chains and the subsequent thermal decomposition of the main (T3) skeleton of polytetrafluoroethylene macromolecules [5]. The amount of coke residue for all studied samples after thermal degradation did not exceed 4 % of their initial mass.

The thermal degradation temperatures of sulfonic acid groups for these membranes range from 350 to 382 °C. The maximum value for this temperature is observed for the LSC-1 membrane without nanoparticles. Regardless of the chemical prehistory of the $Zr_{1-x}Y_xO_{2-0.5x}$ nanoparticles, the degradation temperatures of sulfonic acid groups decrease significantly, reaching a minimum value for the filled sample obtained under hydrothermal conditions. The same sample also demonstrated the highest backbone decomposition temperature compared to the unfilled and composite films. It's worth noting that the T2 and T3 temperatures for the composite membranes correlated with the hydroxyl group content on the surface of the $Zr_{1-x}Y_xO_{2-0.5x}$ nanoparticles, as determined using FTIR spectroscopy. It was shown that the

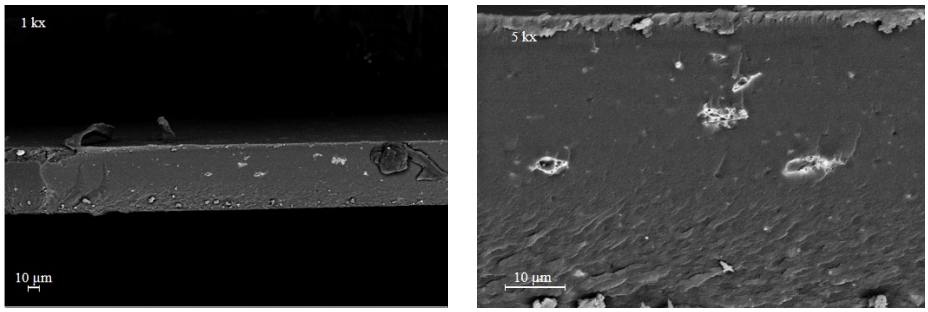

(a)

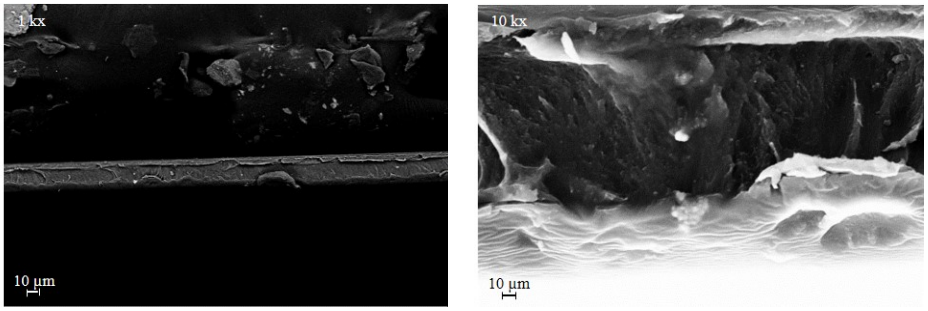

(b)

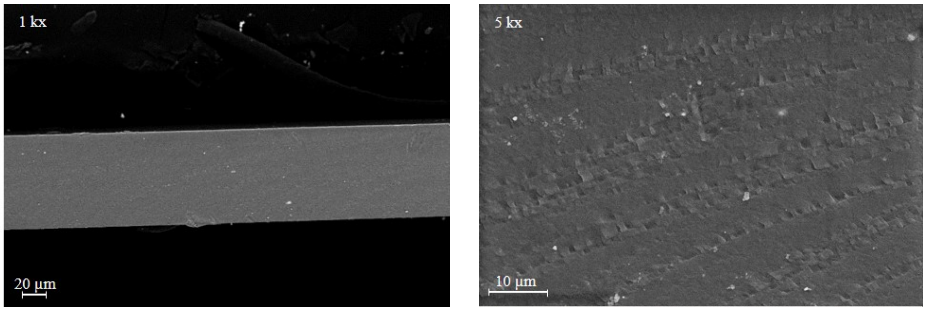

(c)

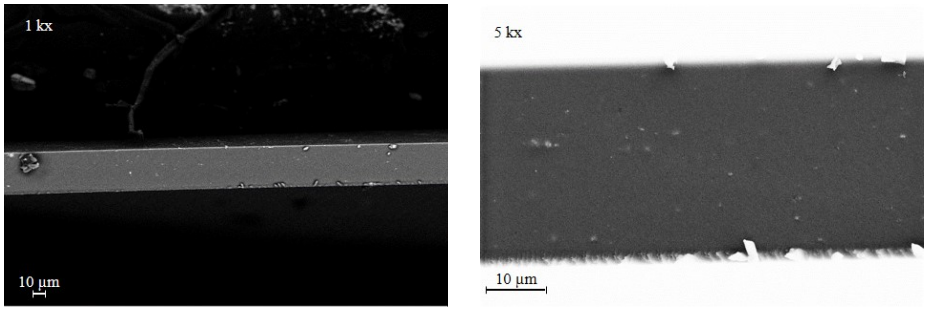

(d)

FIG. 4. SEM cross-section micrographs of the composite films based on perfluorinated polymer and $Zr_{1-x}Y_xO_{2-0.5x}$ nanoparticles obtained by different methods: glycine-nitrate combustion (a), sol-gel (b), hydrothermal (c) and solvothermal (d) syntheses

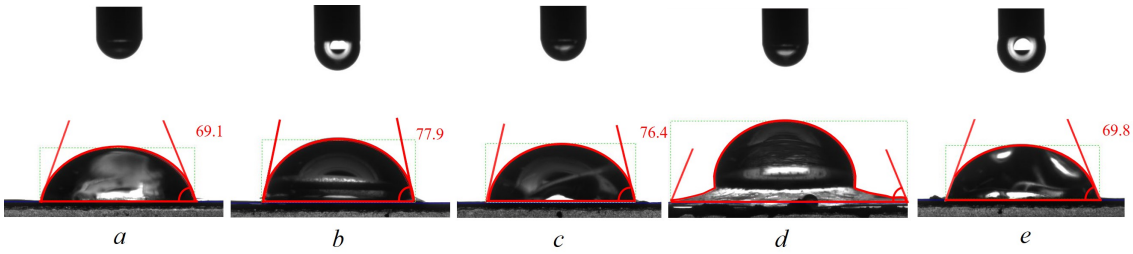

FIG. 5. Image of a droplet when determining the wetting angle of the surface of unfilled (a) and composite films based on a perfluorinated polymer and $Zr_{1-x}Y_xO_{2-0.5x}$ nanoparticles obtained by different methods (glycine-nitrate combustion (b), sol-gel (c), hydrothermal (d) and solvothermal (e) syntheses). Due to instantaneous film swelling of sample d, the value was measured incorrectly

more hydrophobic the surface of the oxide nanoparticles incorporated into the perfluorinated polymer, the higher the degradation temperature of the sulfo-containing fragment and the lower the T3.

TABLE 3. Temperature values of the main stages of mass loss for composite membranes based on perfluorinated copolymer and $Zr_{1-x}Y_xO_{2-0.5x}$ nanoparticles.

Sample	T1	T2	T3
LSC-1	–	382	473
LSC-1 + 0.5 wt. % $Zr_{1-x}Y_xO_{2-0.5x}$ (GNC)	–	373	477
LSC-1 + 0.5 wt. % $Zr_{1-x}Y_xO_{2-0.5x}$ (SG)	–	373	478
LSC-1 + 0.5 wt. % $Zr_{1-x}Y_xO_{2-0.5x}$ (HS)	167	350	518
LSC-1 + 0.5 wt. % $Zr_{1-x}Y_xO_{2-0.5x}$ (SS)	–	369	480

Thermal processes occurring within unfilled and composite membranes during heating were studied using DSC (Fig. 6). For the entire series of samples, two time-extended endothermic effects were observed in the low-temperature region. These effects were caused by the release of adsorbed water from the samples up to 120 °C and the subsequent removal of the amide solvent at temperatures of 120-200 °C. Since the change in the thermal effects of the two aforementioned processes for composite films correlates with the degree of hydrophobicity of the $Zr_{1-x}Y_xO_{2-0.5x}$ nanoparticle surface, it can be confidently concluded that the filler influences the removal of water and DMF from the perfluorinated polymer matrix.

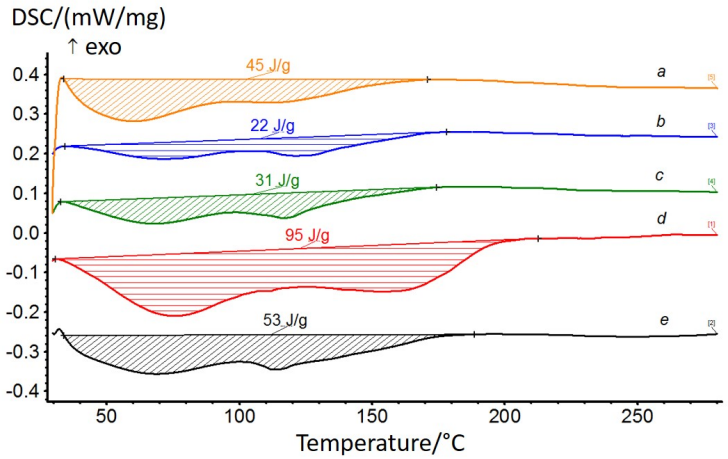

FIG. 6. DSC curves of the first heating of unfilled (a) and composite membranes based on a perfluorinated copolymer and $Zr_{1-x}Y_xO_{2-0.5x}$ nanoparticles obtained under different conditions (glycine-nitrate combustion (b), sol-gel (c), hydrothermal (d) and solvothermal (e) syntheses)

According to XRD data, both the native and composite membranes based on the perfluorinated copolymer have a mesomorphic structure (Fig. 7). Calculation of the crystallinity degree for the unfilled film and samples containing $Zr_{1-x}Y_xO_{2-0.5x}$ nanoparticles with different chemical prehistory yielded virtually identical results. In most cases, the proportion of the crystalline phase was 20 % , with the exception of films with particles obtained using sol-gel technology (25 %) and under hydrothermal conditions (30 %). Therefore, the higher temperature endothermic effect in the DSC curves of composite films is more associated with the removal of solvent from the polymer matrix than with the disordering of chains structured by the filler.

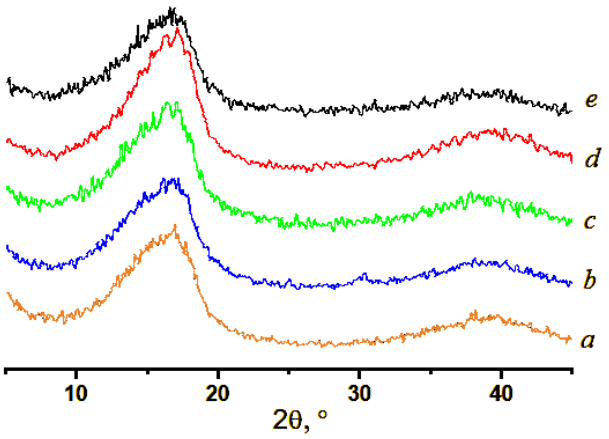

FIG. 7. XRD patterns of unfilled (a) and composite membranes based on perfluorinated polymer and $Zr_{1-x}Y_xO_{2-0.5x}$ nanoparticles obtained by various methods (glycine-nitrate combustion (b), sol-gel (c), hydrothermal (d) and solvothermal (e) syntheses)

The mechanical properties of composite membranes based on the Nafion-type perfluorinated copolymer with $Zr_{1-x}Y_xO_{2-0.5x}$ nanoparticles of varying chemical prehistory were tested using a tensile testing machine in uniaxial tension mode. The characteristics of the tested samples, averaged based on the measurement results, are presented in Table 4, and the type of stress-strain curves themselves are shown in Fig. 8. According to the results of mechanical tests, all films are low-modulus polymeric materials (elastic modulus does not exceed 550 MPa) with deformation at failure in a wide range of values from 30 to 140 % (Table 4). The stress-strain curves of all tested films (Fig. 8) clearly show a transition beyond the plastic limit (a sharp decrease in the slope of the stress-strain curve) at strains of ∼6 – 8 % . The nature of the subsequent deformation process of the tested materials is virtually identical. The curves lack a distinct section of necking through the specimen (as well as a local maximum – the plastic limit). Immediately after strains of 10 – 15 % , a consistent increase in stress begins as the specimens deform, i.e., the so-called strain-hardening region of the material is observed. In all cases, the introduction of ZrO_2-based nanoparticles into the perfluorinated polymer resulted in a decrease in the elastic modulus and plastic limit of the material, along with a significant (2 – 3 times) increase in the ultimate strain before failure (Table 4). In other words, the filler exerts a plasticizing effect on the polymer matrix, apparently by weakening the intermolecular bond system within it.

TABLE 4. Mechanical properties of unfilled and composite films based on a perfluorinated polymer and $Zr_{1-x}Y_xO_{2-0.5x}$ nanoparticles.

Sample	Film thickness, μm	Humidity, %	E, MPa	σ_p, MPa	σ_p, MPa	ε_p, %
LSC-1	58 – 75	54	554±19	16.1±0.7	17.6±0.9	33±4
LSC-1 + 0.5 wt. % $Zr_{1-x}Y_xO_{2-0.5x}$ (GNC)	90	55	466±7	15.7±0.5	19.0±0.8	135±5
LSC-1 + 0.5 wt. % $Zr_{1-x}Y_xO_{2-0.5x}$ (SG)	96-105	54	378±14	14.8±0.5	18.9±0.7	127±9
LSC-1 + 0.5 wt. % $Zr_{1-x}Y_xO_{2-0.5x}$ (HS)	95-105	54	305±16	12.8±0.6	14.4±0.8	70±6
LSC-1 + 0.5 wt. % $Zr_{1-x}Y_xO_{2-0.5x}$ (SS)	98-100	55	325±8	13.1±0.4	15.5±0.4	128±11

$Zr_{1-x}Y_xO_{2-0.5x}$ nanoparticles, synthesized by various methods, were used as a filler for the Nafion-type perfluorinated polymer to enhance its proton conductivity. The surface proton conductivity of unfilled and composite films containing $Zr_{1-x}Y_xO_{2-0.5x}$ nanoparticles was measured at different temperatures using four-probe impedance spectroscopy. It was shown that at room temperature, films containing nanoparticles with the smallest sizes and a more hydrophilic

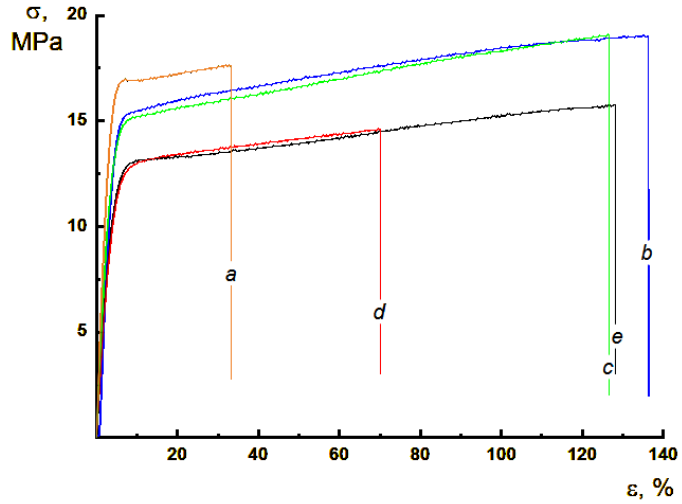

FIG. 8. Strain-strength curves of unfilled and composite films based on perfluorinated polymer and $Zr_{1-x}Y_xO_{2-0.5x}$ nanoparticles obtained by various methods (glycine-nitrate combustion (b), sol-gel (c), hydrothermal (d) and solvothermal (e) syntheses)

surface exhibit the higher proton conductivity, compared to an unfilled membrane (Table 5). In particular, in the case of solvothermal synthesis, the average nanoparticle size was 3 nm, and the surface, due to the process being conducted in a water-alcohol medium, was more hydrophilic than similar particles obtained by other methods. Furthermore, due to the specifics of proton conductivity measurements using the four-probe method, it was important to consider the emergence of nanoparticles on the surface of the perfluorinated polymer and their localization in the near-surface layer, which was only achieved when the filler was produced under solvothermal conditions (Fig. 4d).

Increasing the temperature to 50 °C increased the surface proton conductivity of both the unfilled perfluorinated polymer and its composite membranes with ZrO_2-based nanoparticles. The proton conductivity of the unfilled matrix increased by a factor of 1.5, while that of the composite membranes increased by no more than 1.3. However, the maximum proton conductivity values were still recorded for the LSC-1 + 0.5 wt. % $Zr_{1-x}Y_xO_{2-0.5x}$ (SS) sample, as at room temperature.

TABLE 5. Surface proton-conducting properties of LSC-1 composite membranes with $Zr_{1-x}Y_xO_{2-0.5x}$ nanoparticles obtained by different methods

Sample	Film thickness, μm	Water content, wt. %, 24 hours, 20 °C	Proton conductivity, S/cm RH=100 %	
			23 °C	50 °C
LSC-1	55 – 65	33.0	0.104±0.002	0.152±0.002
LSC-1 + 0.5 wt. % $Zr_{1-x}Y_xO_{2-0.5x}$ (GNC)	80 – 90	32.1	0.122±0.002	0.157±0.009
LSC-1 + 0.5 wt. % $Zr_{1-x}Y_xO_{2-0.5x}$ (SG)	85 – 95	29.3	0.108±0.002	0.145±0.003
LSC-1 + 0.5 wt. % $Zr_{1-x}Y_xO_{2-0.5x}$ (HS)	85 – 95	27.7	0.105±0.007	0.148±0.006
LSC-1 + 0.5 wt. % $Zr_{1-x}Y_xO_{2-0.5x}$ (SS)	85 – 95	33.4	0.134±0.001	0.175±0.001

Measurements of the temperature dependence of the bulk proton conductivity of composite films based on perfluorinated polymer and 0.5 wt. % $Zr_{1-x}Y_xO_{2-0.5x}$ nanoparticles showed that almost all compositions were inferior in this parameter to the unfilled membrane (Fig. 9). At the same time, the range of operating temperatures of the proton-conducting membrane was expanded from 95 to 115 °C due to the introduction of 0.5 wt. % $Zr_{1-x}Y_xO_{2-0.5x}$ (GNC) nanoparticles, which promoted the protection of sulfogroups-containing fragments from premature thermal destruction (Table 3, Fig. 9, dependence b).

Conclusions

Nanoparticles formed in hydrothermal and solvothermal environments are approximately 3 nm in size and contain a large number of hydroxyl groups on the surface, unlike nanoparticles of similar composition synthesized using sol-gel

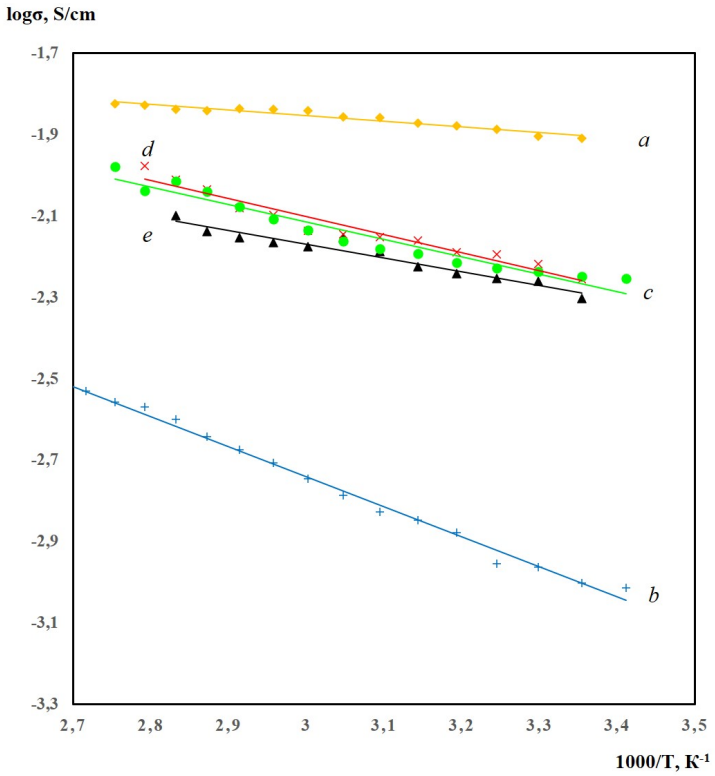

FIG. 9. Temperature dependence of the bulk proton conductivity of unfilled (a) and composite films based on perfluorinated polymer Nafion-type with $Zr_{1-x}Y_xO_{2-0.5x}$ nanoparticles obtained by various methods (glycine-nitrate combustion (b), sol-gel (c), hydrothermal (d) and solvothermal (e) syntheses)

technology or solution combustion. Due to the high synthesis temperatures involved in the latter two methods, particles are larger and have a more hydrophobic surface. Incorporating particles obtained in aqueous and alcohol environments into a perfluorinated copolymer matrix imparted elasticity and increased water retention. This lowered the decomposition temperature of sulfonic acid groups but contributed to an increase in the thermal stability of the main chain. Hydrophilic zirconium dioxide nanoparticles did not aggregate significantly and were uniformly distributed throughout the polymer matrix. Furthermore, surface proton conductivity in membranes containing them was higher than that of composite films with a filler, which had a lower content of hydroxyl groups on the surface. This was particularly noticeable when particles emerged on the surface of the perfluorinated copolymer for LSC-1 + 0.5 wt. % $Zr_{1-x}Y_xO_{2-0.5x}$ (SS). The absolute value of the bulk proton conductivity of all composite membranes was inferior to that of the unfilled perfluorinated copolymer. However, in the case of a sample with nanoparticles synthesized by glycine-nitrate combustion, with a low concentration of OH groups on the surface, it was possible to increase the operating temperature range of such membranes from 95 to 115 °C. It may be promising for the development of membranes for medium-temperature fuel cells.

References

[1] Ketpang K., Son B., Lee D., Shanmugam S. Porous zirconium oxide nanotube modified Nafion composite membrane for polymer electrolyte membrane fuel cells operated under dry conditions. *J. of Membrane Science*, 2015, **488**, P. 154–165.

[2] Mandanipour V., Bemani M., Parsatabar Z. Recent advances in Nafion-based composite membranes for fuel cells: Enhancing performance and durability. *J. Chem. Rev.*, 2026, **8** (1), P. 40–85.

[3] O'Dea J.R., Economou N.J., Buratto S.K. Surface morphology of Nafion at hydrated and dehydrated conditions. *Macromolecules*, 2013, **46** (6), P. 2267–2274.

[4] Zakil F.A., Kamarudin S.K., Basri S. Modified Nafion membranes for direct alcohol fuel cells: An overview. *Renewable and Sustainable Energy Reviews*, 2016, **65**, P. 841–852.

[5] Primachenko O.N., Marinenko E.A., Odinokov A.S., Kononova S.V., Kulvelis Y.V., Lebedev V.T. State of the art and prospects in the development of proton-conducting perfluorinated membranes with short side chains: A review. *Polymers for Advanced Technologies*, 2020, **32** (4), P. 1386–1408.

[6] Okonkwo P.C., Belgacem I.B., Emori W., Uzoma P.C. Nafion degradation mechanisms in proton exchange membrane fuel cell (PEMFC) system: A review. *International J. of Hydrogen Energy*, 2021, **46** (55), P. 27956–27973.

[7] Sigwadi R., Dhlamini M., Mokrani T., Nemavhola F. Wettability and mechanical strength of modified Nafion nanocomposite membrane for fuel cell. *Digest J. of Nanomaterials and Biostructures*, 2017, **12** (4), P. 1137–1148

[8] Karimi M.B., Mohammadi F., Hooshyari K. Recent approaches to improve Nafion performance for fuel cell applications: A review. *International J. of Hydrogen Energy*, 2019, **44** (54), P. 28919–28938.

[9] Kraytsberg A., Ein-Eli Y. Review of advanced materials for proton exchange membrane fuel cells. *Energy and Fuels*, 2014, **28** (12), P. 7303–7330.

[10] Rodriguez J., Rojas N., Sanchez-Molina M., Gonzalez Rodriguez L., Campana R., Rodriguez L. Hybrid membranes based in Nafion-metallic oxides: performance evaluations. *Chemical Engineering Transactions*, 2016, **47**, P. 415–420.

[11] Kim Y., Ketpang K., Jaritphun S., Park J.S., Shanmugam S. A polyoxometalate coupled graphene oxide – Nafion composite membrane for fuel cells operating at low relative humidity. *J. Mater. Chem. A*, 2015, **3**, P. 8148–8155.

[12] Mohanraj V., Kim A.R., Shanmugam R., Yu Y., Yoo D.J. Advanced Nafion nanocomposite membrane embedded with unzipped and functionalized graphite nanofibers for high-temperature hydrogen-air fuel cell system: The impact of filler on power density, chemical durability and hydrogen permeability of membrane. *Composites Part B Engineering*, 2021, **215** (21), 108828.

[13] Liu S., Yu J., Hao Y., Gao F., Zhou M., Zhao L. Impact of SiO_2 modification on the performance of Nafion composite membrane. *Int. J. of Polymer Science*, 2024, **2024** (1), Article ID 6309923, 10 p.

[14] Shao Z.-G., Xu H., Li M., Hsing I-M. Hybrid Nafion–inorganic oxides membrane doped with heteropolyacids for high temperature operation of proton exchange membrane fuel cell. *Solid State Ionics*, 2006, **177** (7), P. 779–785.

[15] Oh K., Kwon O., Son B., Lee D.H., Shanmugam S. Nafion-sulfonated silica composite membrane for proton exchange membrane fuel cells under operating low humidity condition. *J. of Membrane Science*, 2019, **583**, P. 103–109.

[16] Navarra M.A., Abbati C., Scrosati B. Properties and fuel cell performance of a Nafion-based, sulfated zirconia-added, composite membrane. *J. of Power Sources*, 2008, **183** (1), P. 109–113.

[17] Ng W.W., Thiam H.S., Pang Y.L., Chong K.C., Lai S.O. A state-of-art on the development of Nafion-based membrane for performance improvement in direct methanol fuel cells. *Membranes*, 2022, **12** (5), 506.

[18] Ye G., Hayden C.A., Goward G.R. Proton dynamics of Nafion and Nafion/SiO_2 composites by solid state NMR and pulse field gradient NMR. *Macromolecules*, 2007, **40** (5), P. 1529–1537.

[19] Saccà A., Carbone A., Passalacqua E., D'Epifanio A., Licoccia S., Traversa E., Sala E., Traini F., Ornelas R. Nafion–TiO_2 hybrid membranes for medium temperature polymer electrolyte fuel cells (PEFCs). *J. of Power Sources*, 2005, **152**, P. 16–21.

[20] Jian-hua T., Peng-fei G., Zhi-yuan Z., Wen-hui L., Zhong-qiang S. Preparation and performance evaluation of a Nafion-TiO_2 composite membrane for PEMFCs. *International J. of Hydrogen Energy*, 2008, **33** (20), P. 5686–5690.

[21] Yurova P.A., Malakhova V.R., Gerasimova E.V., Stenina I.A., Yaroslavtsev A.B. Nafion/surface modified ceria hybrid membranes for fuel cell application. *Polymers*, 2021, **13** (15), 2513.

[22] Voropaeva D., Merkel A., Yaroslavtsev A. Nafion/ZrO_2 hybrid membranes solvated by organic carbonates. Transport and mechanical properties. *Solid State Ionics*, 2022, **386**, 116055.

[23] Gubanova G.N., Primachenko O.N., Bugrov A.N., Vylegzhanina M.E., Gofman I.V., Lavrentiev V.K., Ivankova E.N., Vlasova E.N., Kononova S.V. Structural and morphological features of perfluorosulfonic acid membranes doped with zirconium dioxide nanoparticles. *J. of Surface Investigation X-ray Synchrotron and Neutron Techniques*, 2024, **17** (S1), P. S391–S403.

[24] Devrim Y., Albostan A. Enhancement of PEM fuel cell performance at higher temperatures and lower humidities by high performance membrane electrode assembly based on Nafion/zeolite membrane. *Int. J. of Hydrogen Energy*, 2015, **40** (44), P. 15328–15335.

[25] Asghar M.R., Zhang W., Su H., Zhang J., Liu H., Xing L., Yan X., Xu Q. A review of proton exchange membranes modified with inorganic nanomaterials for fuel cells. *Energy Adv.*, 2025, **4**, P. 185–223.

[26] Yaroslavtsev A.B., Stenina I.A. Current progress in membranes for fuel cells and reverse electrodialysis. *Mendeleev Commun.*, 2021, **31** (4), P. 423–432.

[27] Saccà A., Carbone A., Gatto I., Pedicini R., Freni A., Patti A., Passalacqua E. Composites Nafion-titania membranes for polymer electrolyte fuel cell (PEFC) applications at low relative humidity levels: Chemical physical properties and electrochemical performance. *Polymer Testing*, 2016, **56** (2), P. 10–18.

[28] Zhu L.-Y., Li Y.-C., Liu J., He J., Wang L.-Y., Lei J.-D. Recent developments in high-performance Nafion membranes for hydrogen fuel cells applications. *Petroleum Science*, 2022, **19**, P. 1371–1381.

[29] Sigwadi R., Mokrani T. Zirconia based/Nafion nanocomposite membranes for fuel cell applications. Proceedings of the 5^{th} International Conference on Nanotechnology: Fundamentals and Applications Prague, Czech Republic, August 11–13, 2014 Paper No. 151.

[30] Almjasheva O.V. Heat-stimulated transformation of zirconium dioxide nanocrystals produced under hydrothermal conditions. *Nanosystems: Physics, Chemistry, Mathematics*, 2015, **6** (5), P. 697–703.

[31] Yamamoto O., Arachi Y., Sakai H., Takeda Y., Imanishi N., Mizutani Y., Kawai M., Nakamura Y. Zirconia based oxide ion conductors for solid oxide fuel cells. *Ionics*, 1998, **4** (5–6), P. 403–408.

[32] Bugrov A.N., Smyslov R.Yu., Zavialova A.Yu., Kopitsa G.P., Khamova T.V., Kirilenko D.A., Kolesnikov I.E., Pankin D.V., Baigildin V.A., Licitra C. Influence of stabilizing ion content on the structure, photoluminescence and biological properties of $Zr_{1-x}Eu_xO_{2-0.5x}$ nanoparticles. *Crystals*, 2020, **10**, 1038.

[33] Bugrov A.N., Almjasheva O.V. Effect of hydrothermal synthesis conditions on the morphology of ZrO_2 nanoparticles. *Nanosystems: Physics, Chemistry, Mathematics*, 2013, **4** (6), P. 810–815.

[34] Bugrov A.N., Smyslov R.Yu., Zavialova A.Yu., Kopitsa G.P. The influence of chemical prehistory on the structure, photoluminescent properties, surface and biological characteristics of $Zr_{0.98}Eu_{0.02}O_{1.99}$ nanophosphors. *Nanosystems: Physics, Chemistry, Mathematics*, 2019, **10** (2), P. 164–175.
[35] Primachenko O.N., Odinokov A.S., Marinenko E.A., Kulvelis Yu.V., Barabanov V.G., Kononova S.V. Influence of sulfonyl fluoride monomers on the mechanism of emulsion copolymerization with the preparation of proton-conducting membrane precursors. *J. of Fluorine Chemistry*, 2021, **244** (4), 109736.
[36] Lutterotti L., Matthies S., Wenk H., Schultz A.S., Richardson J.W. Combined texture and structure analysis of deformed limestone from time-of-flight neutron diffraction spectra. *J. Appl. Phys.*, 1997, **81**, P. 594–600.
[37] Kirilenko D.A., Dideykin A., Aleksenskiy A., Sitnikova A., Konnikov S., Vul' A. One-step synthesis of a suspended ultrathin graphene oxide film: Application in transmission electron microscopy. *Micron*, 2015, **68**, P. 23–26.
[38] Igawa N., Ishii Y. Crystal structure of metastable tetragonal zirconia up to 1473 K. *J. Am. Ceram. Soc.*, 2001, **84** (5), P. 1169–1171.
[39] Martin U., Boysen H., Frey F. Neutron powder investigation of tetragonal and cubic stabilized zirconia, TZP and CSZ, at temperatures up to 1400 K. *Acta Crystallographica Section B*, 1993, **49** (3), P. 403–413.
[40] Tailor S., Singh M., Doub A.V. Synthesis and characterization of yttria-stabilized zirconia (YSZ) nano-clusters for thermal barrier coatings (TBCs) applications. *J. of Cluster Science*, 2016, **27** (4), P. 1097–1107.
[41] Shuklina A.I., Smirnov A.V., Fedorov B.A., Kirillova S.A., Almjasheva O.V. Structure of nanoparticles in the ZrO_2-Y_2O_3 system, as obtained under hydrothermal conditions. *Nanosystems: Physics, Chemistry, Mathematics*, 2020, **11** (6), P. 729–738.

Accepted 8 December 2025

Information about the authors:

Alexander Nikolaevich Bugrov – Branch of Petersburg Nuclear Physics Institute named by B.P. Konstantinov of National Research Centre "Kurchatov Institute" – Institute of Macromolecular Compounds, St. Petersburg, 199004, Russia; Department of Physical Chemistry, Saint Petersburg Electrotechnical University (ETU "LETI"), St. Petersburg, 197022, Russia; ORCID 0000-0003-1052-4919; bugrov.an@mail.ru

Galina Nikolaevna Gubanova – Branch of Petersburg Nuclear Physics Institute named by B.P. Konstantinov of National Research Centre "Kurchatov Institute" – Institute of Macromolecular Compounds, St. Petersburg, 199004, Russia; ORCID 0000-0003-0948-9976; gubanovagn@yandex.ru

Oleg Nikolaevich Primachenko – Branch of Petersburg Nuclear Physics Institute named by B.P. Konstantinov of National Research Centre "Kurchatov Institute" – Institute of Macromolecular Compounds, St. Petersburg, 199004, Russia; ORCID 0000-0003-1637-8537; alex-prima@mail.ru

Iosif Vladimirovich Gofman – Branch of Petersburg Nuclear Physics Institute named by B.P. Konstantinov of National Research Centre "Kurchatov Institute" – Institute of Macromolecular Compounds, St. Petersburg, 199004, Russia; ORCID 0000-0002-1939-2660; gofman@imc.macro.ru

Elena Mikhailovna Ivan'kova – Branch of Petersburg Nuclear Physics Institute named by B.P. Konstantinov of National Research Centre "Kurchatov Institute" – Institute of Macromolecular Compounds, St. Petersburg, 199004, Russia; ORCID 0000-0002-4823-0695; ivelen@mail.ru

Elena Nikolaevna Popova – Branch of Petersburg Nuclear Physics Institute named by B.P. Konstantinov of National Research Centre "Kurchatov Institute" – Institute of Macromolecular Compounds, St. Petersburg, 199004, Russia; ORCID 0000-0001-8470-8994; men682003@mail.ru

Demid Aleksandrovich Kirilenko – Ioffe Institute, St. Petersburg, 194021, Russia; ORCID 0000-0002-1571-209X; demid.kirilenko@mail.ioffe.ru

Victor Konstantinovich Lavrentyev – Branch of Petersburg Nuclear Physics Institute named by B.P. Konstantinov of National Research Centre "Kurchatov Institute" – Institute of Macromolecular Compounds, St. Petersburg, 199004, Russia; ORCID 0000-0002-9930-4666; lavrentev1949@mail.ru

Elena Nikolaevna Vlasova – Branch of Petersburg Nuclear Physics Institute named by B.P. Konstantinov of National Research Centre "Kurchatov Institute" – Institute of Macromolecular Compounds, St. Petersburg, 199004, Russia; ORCID 0000-0002-4644-0445; evl021960@gmail.com

Svetlana Viktorovna Kononova – Branch of Petersburg Nuclear Physics Institute named by B.P. Konstantinov of National Research Centre "Kurchatov Institute" – Institute of Macromolecular Compounds, St. Petersburg, 199004, Russia; ORCID 0000-0001-5468-3909; svetlanavkononova@gmail.com

Conflict of interest: the authors declare no conflict of interest.